Vortex interaction in the wake of a two- and three-bladed wind turbine

Jan Bartl[1], Thomas H. Hansen[2], W. Ludwig Kuhn[3], Franz Mühle[4], Lars Sætran[3]

[1] Dept. of Mechanical and Marine Engineering, HVL, Bergen, Norway

[2] Bergen Offshore Wind Centre, Geophysical Institute, University of Bergen, Norway

[3] Dept. of Energy and Process Engineering, NTNU, Trondheim, Norway

[4] Chair for Wind Energy, Dept. Mech. Eng., TUM, Garching bei München, Germany

E-mail: `jan.bartl@hvl.no`

Abstract. The vortex interaction in the wake behind a two- and three-bladed model scale wind turbine is investigated. The two rotors have equal solidity, and produce similar power and thrust at the design tip speed ratio. Phase-averaged quantities of the wake flow from one to four rotor diameters behind the turbines are measured in a wind tunnel. It is found that the two-bladed turbine has slower wake recovery than the three-bladed turbine, and a larger velocity deficit is produced in the far wake. The tip vortices behind the two-bladed turbine is more stable than behind the three-bladed turbine, and the vortex structures exist further downwind. In a wind farm, this could reduce the power production and increase fatigue loads for the turbines operating in the wake flow, especially during stable atmospheric conditions.

1. Introduction

Given the possible advantages of significantly lower cost and reduced weight, two-bladed wind turbines have recently been given renewed interest for application in the offshore environment. Even though two-bladed turbines have some known disadvantages such as unsteady visual impact and increased noise emissions [1], these drawbacks are of less relevance offshore. Two-bladed rotors are also known to experience higher cyclic loads than three-bladed turbines, and these problems stem from the imbalance of having only two blades when the turbine is exposed to a wind shear or a tower shock impulse [2]. Modern tether connectors and control systems have reduced this problem, and some manufacturers are now developing MW sized two-bladed wind turbines with the ambition of making offshore wind energy more economically attractive [3].

In the classical rotor theory by Glauert, which does not take drag into account, it is shown that a rotor's aerodynamic performance increases with blade number [4]. Today we know that a rotor's highest aerodynamic efficiency is achieved for a low blade number, since this would reduce the total aerodynamic drag [5]. Different studies have investigated how the blade number affects the wind turbine and its wake. In a numerical study performed by Duquette and Visser [6], the effect that the blade number and the rotor solidity has on the turbine performance is investigated. They computed a larger power production for the turbine when increasing the number of blades and applying a large rotor solidity. In another experiment performed by Duquette et al. [7] these findings where partly confirmed, but in contrast to the simulations a decrease in power is observed when the number of blades on the turbine is larger than three.

A different result was obtained in a Computational Fluid Dynamics (CFD) study performed by Newbauer and Kumpaty [8]. They investigated a two-, three- and four-bladed rotor setup and found that the rotor efficiency was reduced with increasing blade number. In a study conducted by Newman et al. [9] the blade number and its effect on the power production for a model scale wind farm was investigated. An analysis of the near wake showed a significant change in mean velocity deficit in the wake behind the turbines using two- or three blades, however, these differences are believed to be influenced by the difference in solidity. From the variety in these results, it is evident that it is not straight forward to make simple conclusions about the aerodynamic efficiency of a wind turbine when the blade number is varied.

In contrast to the effects that the number of blades has on a turbine's performance, acoustic noise and structural integrity, little research on wake interaction effects exists. Since both increased fatigue loads and reduced power production can be linked to the turbulent wake flow impinging on the downstream turbines in a wind farm, wake effects should be considered an indispensable contributor to the cost of energy. The change in wake from altering a turbine's blade number has been investigated by Mühle et al. [10], where the mean and the turbulent wake flow behind a three-bladed and two-bladed rotors is compared. In their study, only the time-averaged flow quantities are analyzed, hence, they could not resolve the tip vortex dynamics in the wake which is considered to be the main driving mechanism behind a wake's decay. To also include this important phenomenon in the present work, a new experiment is set up, where the tip vortex dynamics in a the wake behind a two- and three-bladed rotor is resolved by phase-averaging the measured flow quantities.

As the stability of the tip vortices in a wind turbine's wake is governing its decay, it is currently a central topic in wake research ([11], [12], [13]). The vortices that are shed from the blade tips are known to form a helical vortex system behind the rotor, as shown in Figure 1. Further downstream, the individual vortices begin to interact, break up and merge into turbulent structures. The vortices' stability in the near wake determines the initial state for the wake flow further downstream, a detailed knowledge which is crucial to correctly predict the power and loads on turbines in wind farms. Experimental studies of the tip vortices' interaction and decay have previously been performed by Lignarolo et al. [14], Eriksen and Krogstad [15] and Bastankhah and Porte-Agel [16].
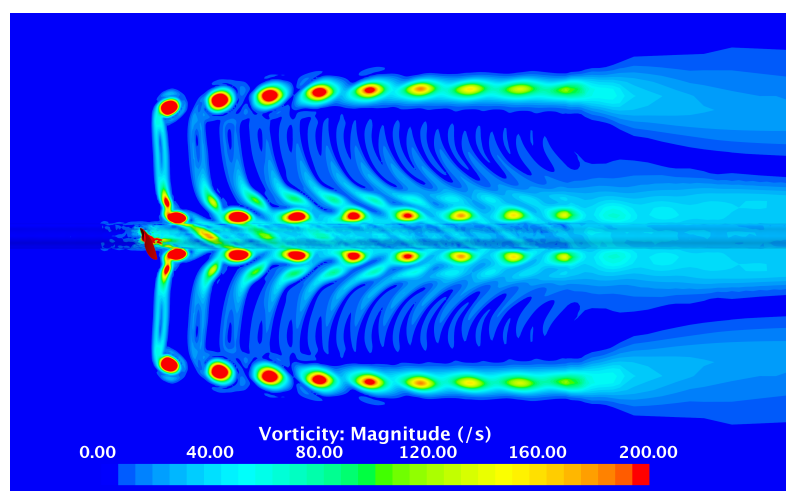
Figure 1. CFD simulation of the instantaneous vorticity behind the two-bladed rotor illustrating the tip vortex helix in the xz-plane.

2. Method

In order to understand how a reduction in blade number from three to two will affect the characteristics of the turbine's wake interaction, an experiment has been performed in the wind tunnel laboratory at the Norwegian University of Science and Technology (NTNU). In the following the methods used to perform the wake experiments are presented, and both the experimental setup and the techniques used to measure the wake flow are described.

2.1. Measurement techniques

The wake flow behind the wind turbines is measured using a setup of two parallel Cobra probes of the type TFI *Series 100*. These four-hole pressure probes are able to acquire all three velocity components. In the probes' heads, four individual pre-calibrated pressure transducers are accommodated. The probe head's geometry limits the measurements to flow angles of $\theta < 45°$. At the downstream measurement locations this criterion is fulfilled. Further information regarding the calibration can be found in Shepherd [17]. Although pressure probes rarely are used for the quantification of tip vortex dynamics, comparative measurements with hot-wire results from Eriksen and Krogstad [15] show a very good agreement in all components of the turbulent stress tensor. The small probe head diameter of $D_{head} = 2.6$ mm is estimated to make out about 4% of the vortex diameter at the initial measurement station one rotor diameter behind the turbine, which is considered sufficient to resolve the structures in the wake. When over-sampled the Cobra probes have a frequency response of $f_{sample} = 10\ kHz$, which is sufficient to capture the phase-averaged turbulent characteristics in the wake flow. The phase-averaged quantities are measured by synchronizing the probes' sampling rate with a pulse defining the rotor's position. For each individual sample a measurement time of $t = 40$ s is applied, corresponding to about 850 rotor rotations. The phase-averaged quantities are calculated by dividing one full rotor revolution into 120 sectors, resulting in a sector size of 3° over which the flow quantities are averaged.

2.2. Measurement locations

The wake behind the two rotor configurations is measured at eleven downstream locations between $x/D = 1.0$ and $x/D = 4.0$ as shown in Figure 2. Most of the results are compared at only six downstream locations ($x/D = 1.2, 1.6, 2.0, 2.6, 3.0, 4.0$) in order to show distinguishable results. Measuring the very near wake at locations $x/D < 1.0$ is not possible, since flow angles $\theta > 45°$ were observed in this region in a preceding experiment (Mühle et al., [18]).
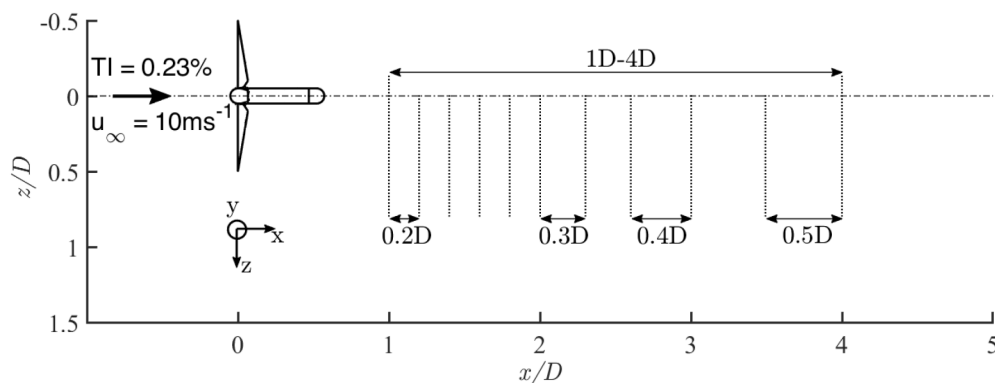
Figure 2. Measurement locations in the wake between $x/D = 1.0$ and $x/D = 4.0$.
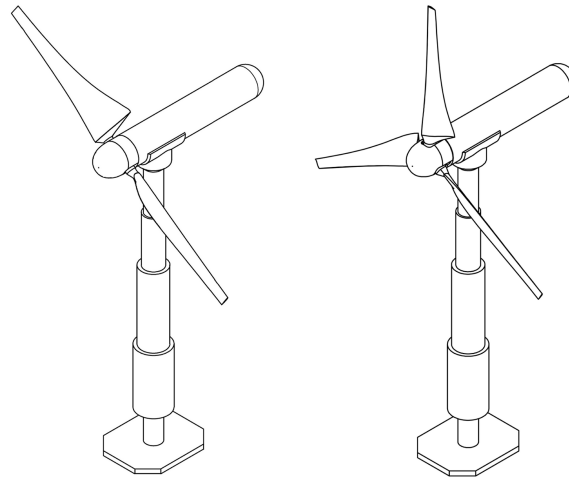
Figure 3. Comparison of the two- and three-bladed model sized wind turbines.

3. Operating conditions

In this section the approach used to design a new rotor blade and airfoil for the two-bladed wind turbine is described. The two-bladed rotor is designed to have similar performance characteristics as an existing three-bladed rotor.

3.1. Rotor design

The two-bladed rotor has a diameter of 0.9 m, and is initially designed as a test platform for a winglet. The details regarding the design of the rotor blade and the airfoil can be found in Hansen and Mühle [19]. The two-bladed rotor is developed using the same design methodology as the equally sized three-bladed wind turbine model developed at NTNU. This three-bladed rotor is originally designed by Krogstad and Lund [20] and is used in a number of experiments, [21], [22], [23], [24], [25]. In the present work the measured performance and wake of the two-bladed and the three-bladed turbine, which are sketched in Figure 3, are compared. The design methodology is therefore briefly explained to show the similarities and the differences between the two turbines. For both turbines, the twist and chord distribution are designed by minimising the axial induction along the rotor blade according to blade element momentum theory. Hence, the fundamental design for both turbines is equal, and the only differences are the number of blades and the airfoil. Both turbines are designed to operate at a tip speed ratio of $\lambda = 6$. The three-bladed turbine uses the *NREL S826* airfoil, and the rotor blades are milled from aluminum. The rotor blades on the two-bladed turbine, however, are 3D-printed from a acrylic material called *Verogray RGD850*, and a new airfoil *Opt* is optimised to ensure that the rotor blades are sufficiently stiff. The new airfoil is designed using the panel code XFOIL and the evolutionary CMA-ES optimisation algorithm. In Figure 4, the two airfoils and their aerodynamic performance are shown. As can be seen, the *Opt* airfoil has better performance and a significantly wider C_l/C_d envelope around $\alpha = 5°$. The chord and twist distribution for the rotors are compared in Figure 5. As can be seen the chord on the two-bladed rotor is larger than on the three-bladed rotor to compensate the loss in solidity from reducing the number of blades on the turbine. The twist distribution is also seen to be different, since the angle of attack for best performance and the lift and drag coefficients are slightly changed on the Opt airfoil compared to S826. The main characteristics of the two rotors are compared in Table 1.

Table 1. Rotor blade geometry specifications

	two-bladed	three-bladed
Rotor diameter	0.9 m	0.9 m
airfoil	Opt	NREL S826
solidity	0.21	0.21
tip chord length	39.7 mm	25.8 mm
twist angle at tip	1.54°	−0.72°
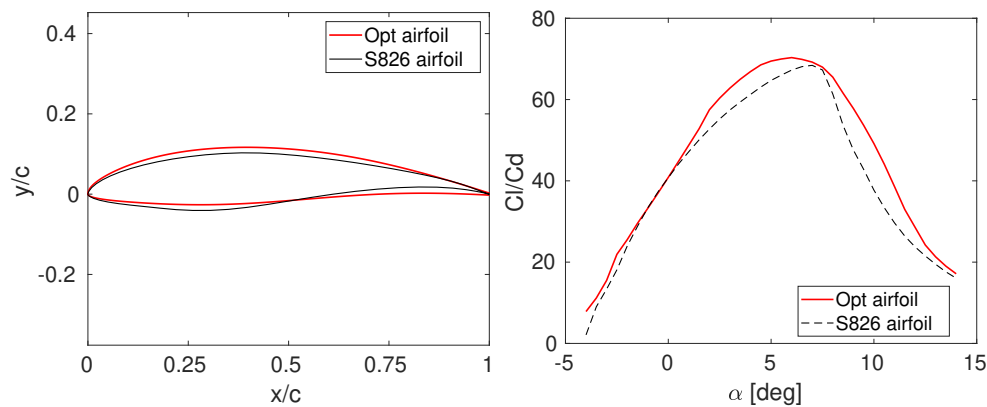
Figure 4. Comparison of the *Opt* airfoil (two-bladed rotor), the NREL S826 airfoil (three-bladed rotor) and their lift-to-drag-coefficients.

3.2. Turbine performance
The power and thrust characteristics of both rotors were measured with a torque and rpm sensor, as well as a force balance, respectively. The results are shown in Figure 6. The power coefficient is seen to be very similar for both rotors up until $\lambda = 4$, while consistent larger power coefficient is measured for the two-bladed design at higher tip speed ratios. This is assumed to be a result of the previously shown wider C_l/C_d envelope of the *Opt* airfoil. The measured thrust is seen to be very similar for both rotors.
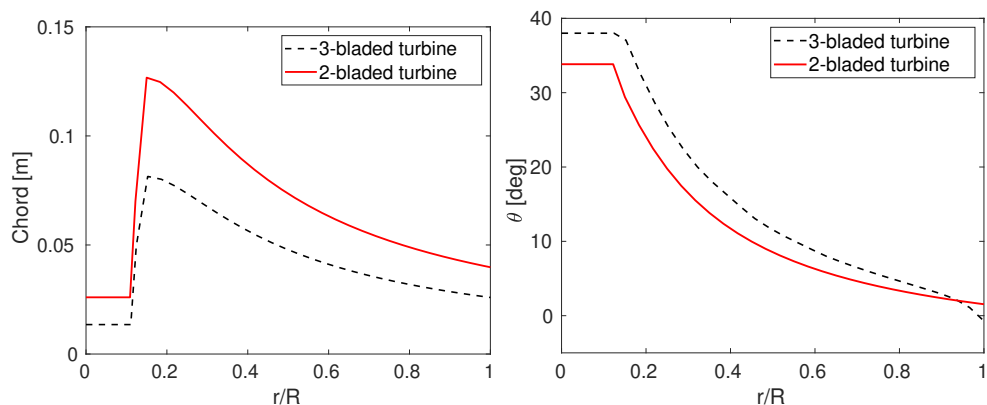
Figure 5. Comparison of the two- and three-bladed rotor's chord and twist distribution.
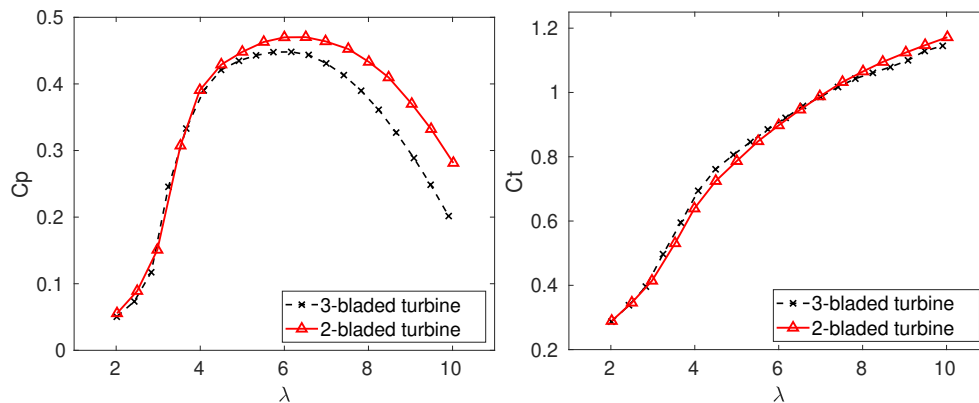
Figure 6. Comparison of the two- and three-bladed rotor's measured power coefficient C_P and thrust coefficient C_T in dependency of its tip speed ratio.

4. Results

In this section the results of the time-averaged, and phase-averaged quantities in the wake behind the two rotors are compared.

4.1. Time-averaged streamwise velocity

At first, the measurements of the time-averaged streamwise velocity in the wake behind the two- and three-bladed rotor are compared. A look into selected cross-sectional cuts, as presented in Figure 7, shows a higher initial (at $x/D = 1.2$) velocity deficit in the blade tip region from $z/D = 0.5 - 0.6$ behind the three-bladed rotor. As the wake progresses further downstream, the differences in the velocity deficits behind the two rotors are observed to be very similar at $x/D = 2.0$. Proceeding even further downstream to the transition region between near and far wake at $x/D = 4.0$ the velocity deficit in the three-bladed wake becomes even smaller than the deficit in the two bladed wake. As the development of the mean streamwise velocity in the wake is not intuitively explainable, the total kinetic energy as well as phase-averaged quantities are analysed.
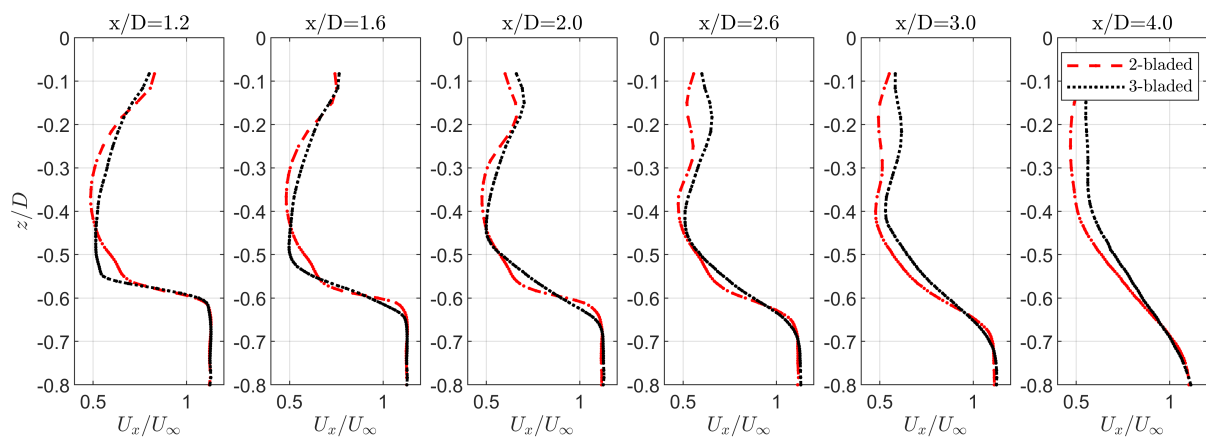
Figure 7. Comparison of cross-sectional cuts of the time-averaged streamwise velocity.
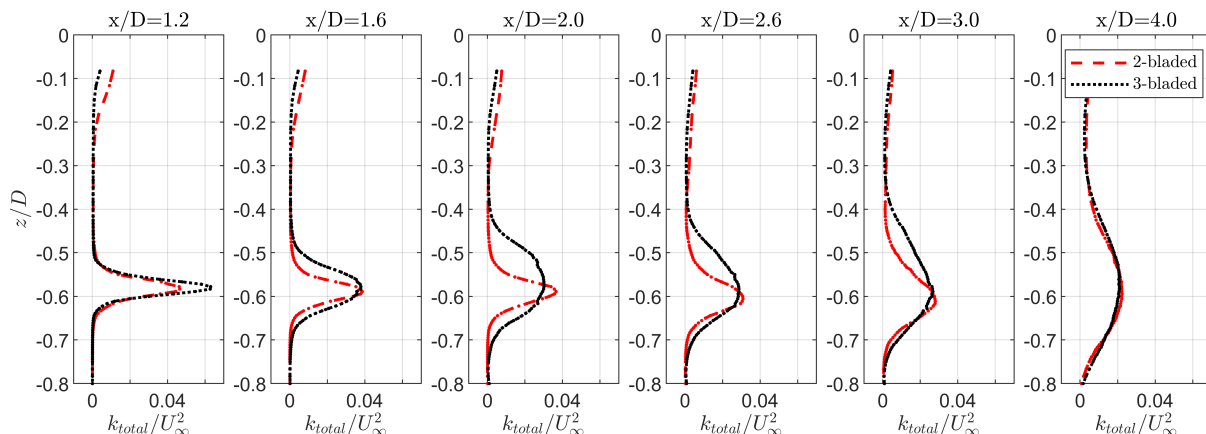
Figure 8. Comparison of cross-sectional cuts of the time-averaged total kinetic energy.

4.2. Time-averaged total kinetic energy

The kinetic energy in the tip region of the near wake behind a wind turbine rotor is dominated by coherent periodic motions rather than by random turbulent motions. For this reason we use the term *total kinetic energy* rather than *turbulent kinetic energy* here. According to the triple decomposition method described in Cantwell and Coles [26] the single stress components are resolved into a contribution from the periodic motion and a contribution from the random motion at specific phase $k_{total} = \frac{1}{2}(\widetilde{u_i \widetilde{u}_i} + \overline{u'_i u'_i})$. Herein, $\widetilde{u_i \widetilde{u}_i}$ is the contribution from the periodic part and $\overline{u'_i u'_i}$ denotes the random fluctuation of the velocity components. The time-averaged non-dimensional total kinetic energy in the wake behind the two rotor setups is shown in Figure 8. Comparing the wake's total kinetic energy profiles, higher initial kinetic energy levels are observed in the tip region behind the three-bladed configuration in the near wake at $x/D = 1.2$. The initial width of the tip vortex is observed to be very similar for the two- and three bladed rotor. Already at $x/D = 1.6$, however, the kinetic energy peak in the wake of the three-bladed rotor has become wider than the peak behind the two-bladed configuration. As the wake progresses further downstream the kinetic energy in the tip region spreads out laterally significantly faster for the three-bladed configuration. At $x/D = 2.0$ the total kinetic energy peak behind the three-bladed rotor is approximately double as wide as the one behind the two-bladed configuration. Approaching the transition region from near- to far-wake at $x/D = 4.0$ the kinetic energy profiles behind both rotors are observed to be very similar, spreading over a wide spanwise range from about $z/D = 0.2 - 0.8$. The largest differences in the total kinetic energy distributions are observed for downstream distances ranging from about $x/D = 1.6$ to $x/D = 3.0$. To get a better understanding of the mechanism governing the observed mean streamwise velocity and total kinetic energy distributions, the phase-averaged quantities are analysed.

4.3. Phase-averaged turbulent kinetic energy

As described in Section 2.1, the sampling frequency of the Cobra-probes measuring the wake flow was synchronized with the rotational speed of the two rotors. This allowed us to extract all measured quantities for a specific rotor phase from $\theta = 0 - 360°$. All quantities are binned into 120 sectors, using a sector size of $3°$. This makes it possible to calculate the phase-average for each quantity, for each sector. This process isolates the coherent motions of the tip vortices from random turbulent fluctuations in the wake. The results of the phase-averaged turbulent kinetic energy in the tip vortex region of the wake behind the two rotors is presented for six selected
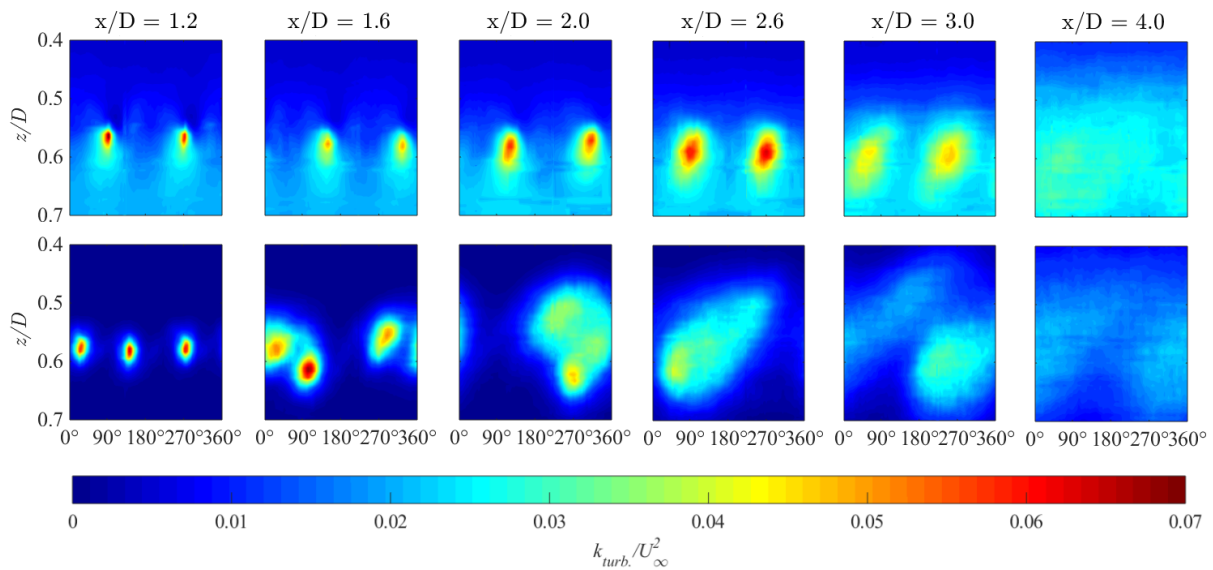
Figure 9. Comparison of the phase-averaged turbulent kinetic energy measured at different downstream locations from $x/D = 1.2$ to $x/D = 4.0$ in the wake behind the two-bladed (upper row) and three-bladed rotor (lower row).

downstream locations in Figure 9. A quantification of the exact turbulent kinetic energy levels is given in Figure 10, in which the peak levels are extracted from the phase-averaged vortex cores for both rotor configurations. It is evident that the turbulent kinetic energy strongly varies for the different rotor phases. High levels of turbulent kinetic energy are only observed for rotor phases when a tip vortex passes the measurement location. Up until the first downstream measurement location at $x/D = 1.2$ the vortex spirals behind both rotors are observed to be stable. Two, and three vortex cores are clearly identified, having a rather constant inter-vortex-distance h_V to each other. The vortex core TKE levels are measured to be at a comparable level for both rotor types. Already at $x/D = 1.6$, however, an obvious differences between the two rotor configurations is observed. While the tip vortices shed from the two-bladed rotor still travel
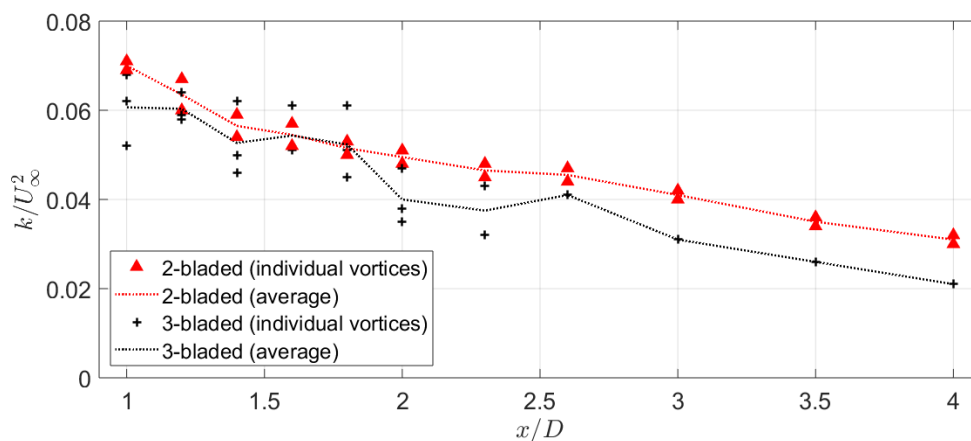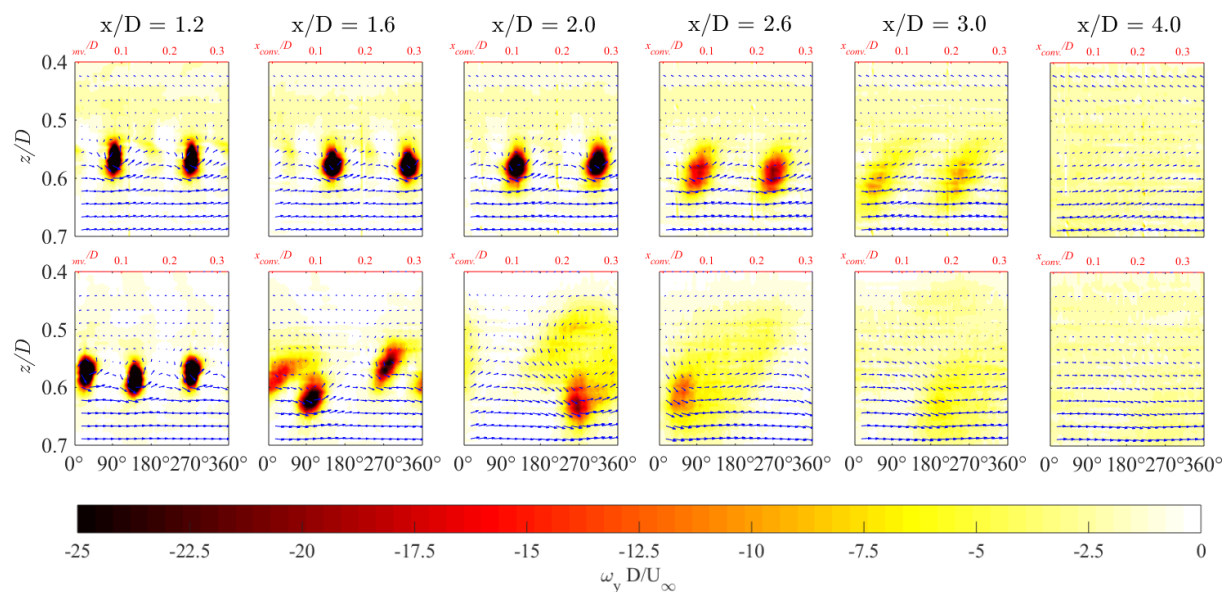

Figure 10. Comparison of the maximum core turbulent kinetic energy extracted from the single vortex cores in the wake behind the two-bladed and three-bladed rotor.

downstream in ordered spirals, the vortices behind the three-bladed rotor interact. The single vortices starts to wrap around each other, which results in lateral vortex displacement. At the same time their streamwise inter-vortex-distance h_V is significantly reduced. As a consequence of the lateral vortex displacement, the time-averaged total kinetic energy, as previously depicted in Figure 8, is observed to form a significantly broader shear layer behind the three-bladed rotor than behind the two-bladed rotor from $x/D = 1.6$ on. At the downstream distance of $x/D = 2.0$ the three vortices shed from the three-bladed rotor are observed to be in the process of merging into a single structure. One of the vortex cores is carrying more turbulent kinetic energy than the other cores, and they get completely wrapped around each other. In contrast to that, the clearly defined vortices behind the two-bladed rotor are still keeping their distance at this downstream distance. Even further downstream at $x/D = 2.6 - 3.0$ distinct vortex spirals of stable distance are observed for the two-bladed configuration, while the three vortices behind the three-bladed rotor have merged into a single turbulent structure. The vortex core TKE levels are observed to be significantly higher for the more stable two-bladed configuration at this downstream location. At $x/D = 4.0$ the turbulent kinetic energy is seen to be more uniformly spread out over all rotor phases for the three-bladed configuration, indicating that the coherent vortical structures have decayed into turbulence at this downstream distance. Also for the two-bladed configuration the turbulent kinetic energy is uniformly distributed over all rotor phases at $x/D = 4.0$, featuring about 50% higher TKE levels than behind the three-bladed rotor. In contrast to the three-bladed rotor, no obvious vortex wrapping process has been observed for the two bladed case.

4.4. Phase-averaged vorticity

The vortices' strength and rotation is further studied by analysing the phase-averaged, out-of-plane vorticity $\langle \omega_y \rangle$. The out-of-plane vorticity component is defined by the partial spatial derivations of the two in-plane velocity components: $\langle \omega_y \rangle = \langle \partial u_x / \partial z - \partial u_z / \partial x \rangle$. For an estimation of the local velocity component u_x, the vortices' convective velocity has to

Figure 11. Comparison of the phase-averaged vorticity calculated at different downstream locations from $x/D = 1.2$ to $x/D = 4.0$ in the wake behind the two-bladed (upper row) and three-bladed rotor (lower row).
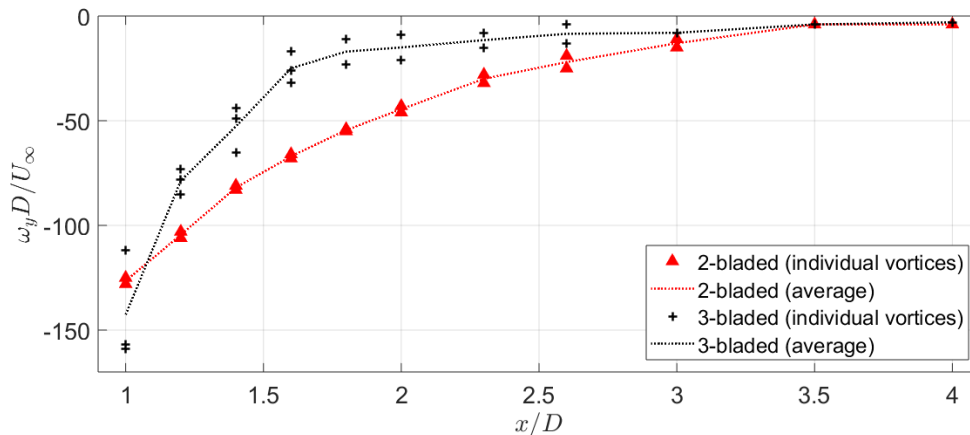
Figure 12. Comparison of the maximum core vorticity extracted from the individual vortex cores in the wake behind the two-bladed and three-bladed rotor.

be subtracted from the measured total streamwise velocity in the wake $u_x = U_x - U_{conv}$. Applying Taylor's frozen equilibrium approximation $\Delta x \approx U_{conv}\Delta\tau$ the time derivatives can be transformed to spatial derivatives which are needed for the calculation of the local vorticity. The convective velocity U_{conv} is calculated from the local mean velocity at the inner border of the shear layer between z/D=0.55-0.60, averaged over all rotor phases for both configurations. The phase-averaged out-of-plane vorticity is depicted in Figure 11 for both rotor setups. The color contours indicate the non-dimensional vorticity, while the in-plane velocity field is depicted by the blue vectors formed by u_x and u_z at the six selected downstream locations. In addition to the rotor phase, the calculated convective distance x_{conv} is shown on an additional x-axis. In general, the locations of high vorticity coincide with the previously discussed locations of increased turbulent kinetic energy. The vectors in the xz-plane indicate low vorticity inside the vortex helix. In addition, a strongly negative rotation around the vortex cores as well as aligned flow along the x-axis in the freestream region outside the wake helix is observed. The chosen vector grid does not resolve minor vortical structures in the interaction region behind the three-bladed rotor at $x/D = 2.0$, but indicates that the three vortices have merged into a larger vortical structure with negative rotation. The vorticity study thus confirms the persistently stable helix behind the two-bladed setup up until $x/D = 3.0$. The vortex cores are observed to become weaker, slightly larger and deflected outwards with increasing downstream distance. At $x/D = 4.0$ no clear vortex cores could be detected behind both rotors, with a low-level vorticity being spread out over all rotor phases. As the level of the non-dimensional peak vorticity decreases strongly from $x/D = 1.0$ to $x/D = 4.0$ the chosen color scale in Figure 11 is a trade-off. An accurate quantification of the vorticity magnitude extracted from the phase-averaged vortex cores is given in Figure 12 for both rotor configurations. The initial levels of core vorticity are observed to be similar at $x/D = 1.0$, although a significant variation in core vorticity between the single vortices shed from the three-bladed rotors are observed. Within the downstream range from $x/D = 1.2$ to $x/D = 3.0$, the core vorticity levels in the wake of the three-bladed rotor are consistently lower than in the wake of the two-bladed turbine. It has to kept in mind that the total vorticity in the wake is the sum of the vorticity from all tip vortices shed from the wind turbine rotor blades. Hence, the total vorticity levels would be equal for the turbine with two- and three rotor blades. However, for a wind turbine operating in the wake flow, the more defined vortices shed from the two-bladed rotor could lead to higher fatigue loads.

Keeping in mind that the total generated vorticity in the wake consists of the sum of the

two respectively three shed vortices, the total vorticity levels in this region would be similar for both configurations. Further downstream, at $x/D > 3.0$ the vorticity levels are measured to be equally low for both configurations, as the vortex cores basically have decayed into turbulence.

5. Discussion

The results from this study are only valid for the applied boundary conditions in the wind tunnel experiments, since increasing the inlet turbulence levels or the Reynolds number will result in a faster wake recovery. In the present experiment the rotors' solidity and design tip speed ratio is kept equal, and this results in larger chord sizes for the two-bladed when using the same operational design tip speed ratio. Another option for the two-bladed rotor's design would have been to use a higher tip speed ratio. This would thus reduce the chord size in order to keep the solidity equal.

Similar experimental studies of vortex interaction using particle-image-velocimetry behind either two- and three bladed rotors have been performed by Lignarolo et al. [14], Bastankhah and Porté-Agel [16]. Lignarolo et al.'s study of the wake behind a two-bladed model turbine of $D = 0.60$ m investigated the pair-wise vortex interaction dependent on the tip speed ratio. For their turbine's design tip speed ratio $\lambda = 6.0$, a vortex pairing could already be observed around $x/D = 1.5$, while a reduction in tip speed ratio to $\lambda = 4.8$ delayed the instability to approximately $x/D = 1.8$. The vortices in the two-bladed rotor's wake in the present experiment, however, are seen to be more stable over time and travel further downstream. A higher inflow turbulence in Lignarolo et al.'s experiment, as well as a different rotor design could have caused these differences. A small three-bladed rotor of $D = 0.12$ m with straight wing tips was used by Bastankhah and Porté-Agel [16] to investigate the tip vortices's stability. An analysis of the phase-averaged vorticity showed that an identification of the location of the initial instability was not straight forward. A meandering wake was observed in their experiment, due to the small size of the rotor with respect to turbulent length scales in the inflow.

6. Conclusions

An experimental study of the wake flow behind a two- and three-bladed model wind turbine rotor is performed. The two rotors have similar solidity, power and thrust characteristics when operated at the design tip speed ratio. An analysis of the mean streamwise velocity in the wake revealed a slightly higher initial velocity deficit in the tip region behind the three-bladed rotor. As the wake develops downstream, however, the velocity deficit behind the three-bladed rotor gradually becomes smaller than the deficit behind the two-bladed rotor. A similar observation has been made in the downstream development of the coherent and turbulent kinetic energy in the tip region. Initially higher kinetic energy peaks behind the three-bladed rotor are seen to broaden up and decay at a faster rate compared to the peaks in the two-bladed rotor's wake. These observations could be ascribed to a significantly earlier interaction and decay of the tip vortices in the wake of the three-bladed rotor. In the downstream region between $x/D = 1.6$ and $x/D = 3.0$, the vortices shed from the three-bladed rotor paired and merged into a single structure. In the same downstream region the two-bladed rotor's vortices were seen to continue moving downstream in an ordered helix. The higher inter-vortex-distance is assumed to be the main cause for the delayed decay in the wake of the two-bladed rotor.

Under the present boundary conditions of this experiment, the wake recovery behind the two-bladed rotor is observed to be delayed compared to a three-bladed turbine. In a stable atmosphere, this could cause a lower power output and higher fatigue loads on a potential downstream turbine in a full-scale wind farm. However, the influence of certain rotor design parameters, such as solidity, aspect ratio, design tip speed ratio or blade tip geometry, were not investigated in this study. These parameters could potentially affect the wake development significantly and will be investigated in future research.

Data availability

Numerical simulations of this study and further parameter variations are highly encouraged. The rotor design files, wind tunnel boundary conditions and all experimental results presented in this paper can be accessed via *https://doi.org/10.5281/zenodo.3751104* [27].

References

[1] Hau E 2006 *Wind Turbines. Fundamentals, Technologies, Application, Economics.* (Springer)
[2] Jamieson P 2011 *Innovation in wind turbine design* (John Wiley and Sons)
[3] Caruso S and Avolio S 2019 *Wind Europe Conference and Exhibition, Bilbao*
[4] Glauert H 1935 *Aerodynamic Theory Volume IV, Division L, Dover Publications Inc* 169–360
[5] Almukhtar A 2012 *Energy Procedia* **18** 404–415
[6] Duquette M and Visser K 2003 *Journal of Solar Energy Engineering* **125** 425–432
[7] Duquette M, Swanson J and Visser K 2003 *Wind Engineering* **27** 299–316
[8] Newbauer S and Kumpaty S 2012 *Proceedings of the ASME 2012 International Mechanical Engineering Congress and Exposition* IMECE2012–85557
[9] Newman A, Cal R and Castillo L 2015 *Renewable Energy* **81** 472–481
[10] Mühle F, Adaramola M and Sætran L 2016 *Journal of Physics: Conference Series* **753** 032017
[11] Sørensen J N 2011 *Journal of Fluid Mechanics* **682** 1–4
[12] Sarmast S, Dadfar R, Mikkelsen R F, Schlatter P, Ivanell S, Sørensen J N and Henningson D S 2014 *Journal of Fluid Mechanics* **755** 705–731
[13] Okulov V, Kabardin I, Mikkelsen R, Naumov I and Sørensen J N 2019 *Journal of Fluid Mechanics* **859** 1084–1097
[14] Lignarolo L, Ragni D, Krishnaswami C, Chen Q, Simao Ferreira C and van Bussel G 2014 *Renewable Energy* **70** 31–46
[15] Eriksen P E and Krogstad P Å 2017 *Renewable Energy* **108** 449–460
[16] Bastankhah M and Porté-Agel F 2017 *Physics of Fluids* **29** 065105
[17] Shepherd I C 1981 *Journal of Fluids Engineering* **103** 590–594
[18] Mühle F, Bartl J, Hansen T, Adaramola M and Sætran L 2020 *Wind Energy (in review)*
[19] Hansen T H and Mühle F 2018 *Wind Energy* **21** 634–649
[20] Krogstad P and Lund J 2012 *Wind Energy* **15** 443–457
[21] Krogstad P and Eriksen P 2013 *Renewable Energy* **50** 325–333
[22] Pierella F, Krogstad P and Sætran L 2014 *Renewable Energy* **70** 62–77
[23] Krogstad P, Sætran L and Adaramola M 2015 *Journal of Fluids and Structures* **52** 65–80
[24] Bartl J and Sætran L 2017 *Wind Energy Science* **2** 55–76
[25] Mühle F, Schottler J, Bartl J, Futrzynski R, Evans S, Bernini L, Schito P, Draper M, Guggeri A, Kleusberg E, Henningson D, Hölling M, Peinke J, Adaramola M and Sætran L 2018 *Wind Energy Science* **3** 883–903
[26] Cantwell B and Coles D 1983 *Journal of Fluid Mechanics* **136** 321–374
[27] Bartl J, Hansen T and Mühle F 2020 *Zenodo, http://doi.org/10.5281/zenodo.3751104*